remote sensing

MDPI

Article

SNR (Signal-To-Noise Ratio) Impact on Water Constituent Retrieval from Simulated Images of Optically Complex Amazon Lakes

Daniel S. F. Jorge *, Claudio C. F. Barbosa, Lino A. S. De Carvalho, Adriana G. Affonso, Felipe De L. Lobo and Evlyn M. L. De M. Novo

National Institute for Space Research, Avenida dos Astronautas, 1758, São José dos Campos, SP 12227-010, Brazil; claudio.barbosa@inpe.br (C.C.F.B.); lino@dsr.inpe.br (L.A.S.D.C.); affonso@dsr.inpe.br (A.G.A.); felipe.lobo@inpe.br (F.D.L.L.); evlyn.novo@inpe.br (E.M.L.D.M.N.)

* Correspondence: danielsfj@dsr.inpe.br; Tel.: +55-11-94982-6778

Academic Editors: Yunlin Zhang, Claudia Giardino, Linhai Li, Deepak R. Mishra and Prasad S. Thenkabail
Received: 26 February 2017; Accepted: 19 June 2017; Published: 22 June 2017

Abstract: Uncertainties in the estimates of water constituents are among the main issues concerning the orbital remote sensing of inland waters. Those uncertainties result from sensor design, atmosphere correction, model equations, and in situ conditions (cloud cover, lake size/shape, and adjacency effects). In the Amazon floodplain lakes, such uncertainties are amplified due to their seasonal dynamic. Therefore, it is imperative to understand the suitability of a sensor to cope with them and assess their impact on the algorithms for the retrieval of constituents. The objective of this paper is to assess the impact of the SNR on the Chl-a and TSS algorithms in four lakes located at Mamirauá Sustainable Development Reserve (Amazonia, Brazil). Two data sets were simulated (noisy and noiseless spectra) based on in situ measurements and on sensor design (MSI/Sentinel-2, OLCI/Sentinel-3, and OLI/Landsat 8). The dataset was tested using three and four algorithms for TSS and Chl-a, respectively. The results showed that the impact of the SNR on each algorithm displayed similar patterns for both constituents. For additive and single band algorithms, the error amplitude is constant for the entire concentration range. However, for multiplicative algorithms, the error changes according to the model equation and the R_{rs} magnitude. Lastly, for the exponential algorithm, the retrieval amplitude is higher for a low concentration. The OLCI sensor has the best retrieval performance (error of up to 2 μg/L for Chl-a and 3 mg/L for TSS). For MSI, the error of the additive and single band algorithms for TSS and Chl-a are low (up to 5 mg/L and 1 μg/L, respectively); but for the multiplicative algorithm, the errors were above 10 μg/L. The OLI simulation resulted in errors below 3 mg/L for TSS. However, the number and position of OLI bands restrict Chl-a retrieval. Sensor and algorithm selection need a comprehensive analysis of key factors such as sensor design, in situ conditions, water brightness (R_{rs}), and model equations before being applied for inland water studies.

Keywords: signal-to-noise ratio; Remote Sensing Reflectance; bio-optical algorithms; inland waters

1. Introduction

Sensor design (spatial, radiometric, and spectral resolution, and signal-to-noise ratio-SNR) is shaped by remote sensing applications (satellite mission). During the last decade, most sensors in orbit were designed for either oceanic water or land applications (e.g., Moderate Resolution Imaging Spectroradiometer (MODIS) Aqua and Terra). Therefore, they were not tuned for inland water applications. Despite numerous studies focusing on inland waters, these sensors are suboptimal, imposing an intense impact on the estimate accuracy [1].

A sensor's SNR is a major issue for the remote sensing community since a large part of the signal comes from atmospheric interference which increases noise. The maximum contribution of the water leaving radiance to the measured signal at the sensor is about 15% [2], whereas the remainder comes from the atmosphere [3–5]. Despite advances in atmospheric correction, residual atmospheric noise remains [6,7]. The SNR of an orbital sensor, measured in the laboratory, can be based on a standard target. A spectrally uniform 5% albedo is commonly used during laboratory calibration with sensors designed for water measurements [8]. However, water leaving radiance is usually lower than that, especially in the longer wavelengths and in waters dominated by organic matter; thus, the actual SNR may fail to reach the prescribed SNR [6,8,9]. The application of orbital sensors to inland waters with low radiance can be highly affected by sensor noise. Degradation of the spatial resolution is usually applied as a tool to reduce noise, thus overcoming SNR limitations. Vanhellemont & Ruddick [10] described the relation between SNR and spatial resolution for Operational Land Imager (OLI) and MODIS images, demonstrating how resampling can reduce the noise in the red band. Regarding the study of small lakes, where only a few pixels are available and resampling is not feasible, the SNR impact is critical. Spectral resolution also impacts the SNR, as the narrower the band width is, the more sensitive it is to the absorption peaks. However, to maintain the SNR requirements for water applications, a sensor´s spatial resolution is compromised, since the narrower the bandwidth, the higher the noise. This aspect is observed by comparing the SNR of multispectral and hyperspectral sensors [6,7,11].

In the earliest stages of remote sensing, sensors designed for water color retrieval proved to be very effective for open ocean waters (e.g., IOCCG [12] and Muow et al. [13]). However, monitoring inland waters is more challenging, because of their optical complexity, high spatial frequency of water components, and sensor constraints [14]. New sensors made available in the last few years, such as the Multispectral Instrument (MSI), Ocean and Land Color Instrument (OLCI), Operational Land Imager (OLI), and Hyperspectral imager for the Coastal Ocean (HICO) are potentially useful for inland water studies. The selection of the best sensor, however, is a challenging task because of the limited number of studies regarding the impact of sensor design on inland water color product uncertainty. Gerace et al. [15] compared the quality of four sensors for deriving bio-optical products applied to coastal water studies and concluded that SNR and spatial resolution are the sensor design features with the largest impact on bio-optical product uncertainty. Similarly, Moses et al. [8] focused on the SNR impact on HICO data quality, but only provided information about the average impact of the SNR on the bio-optical products, without assessing how differences in the model equations (additive and/or multiplicative operations and linear or logarithmic fit), magnitude, and shape of each R_{rs} spectrum contributed to the relative impact of SNR on product uncertainty.

The uncertainties in the R_{rs} spectrum related to sensor design can also be further amplified depending on the target characteristics. In the case of the Amazon floodplain lakes, those uncertainties can be even larger because they are usually isolated, surrounded by dense vegetation characterized by very high trees (up to 35 m) and subjected to seasonal variation in size, depth, and optical composition due to the Flood Pulse [16]. In addition to these threshold constraints related to inland waters, atmospheric correction in the Amazon region can be another major source of uncertainty due to the spatial and temporal variation of cloud cover, including cloud shadow and aerosol scattering properties [10]. To successfully obtain water color products in these challenging conditions, it is crucial to assess the intrinsic capability of the available sensors and quantify their impact on the water leaving signal and water color algorithms.

Given this lack of information concerning the uncertainties caused by the interplay of sensor design and target optical features, the objective of this paper is to assess the impact of the SNR on water color products derived from satellite images applied in threshold conditions such as the Amazon floodplain lakes. To accomplish this objective, optical and limnological in situ measurements were collected at Mamirauá Sustainable Development Reserve (RDSM), in Central Amazon, Brazil,

and used as the input to simulate three orbital image sensors (MSI/Sentinel-2, OLCI/Sentinel-3, OLCI/Landsat 8).

2. Materials and Methods

2.1. Study Site Description

The selected lakes are located in the RDSM (Figure 1a,b). This is the first and largest Sustainable Development Reserve in Brazil dedicated exclusively to the protection of the Amazonian floodplain, comprising approximately 1,124,000 hectares. This Conservation Unit was created by the State of Amazonas in 1996 and is one of the Brazilian sites of the United Nations Ramsar Convention [17]. It consists of a pristine floodplain inundated by sediment-rich whitewater rivers at the confluence of the Japurá and Solimões rivers, and forms a complex mosaic of seasonally flooded forests, lakes, and channels. Rivers and lakes undergo constant change due to the transport of sediments and organic matter, caused by the annual water level variation of up to 12 m [17–20]. Moreover, the seasonal flooding changes the proportion of suspended and dissolved components in the water by altering its physical-chemical conditions [21]. Consequently, this affects the ecosystem where these waters circulate [22]. The flood pulse starts in May and ends in July, while the drought period lasts from September to November. The rising of the water level begins in January and the water starts receding in September. The flood pulse has a monomodal annual pattern (Figure 1c), and the changes in the water level are due to changes in the snowmelt in the Andes and precipitation in the pre-andean region and in the median Amazon basin [19]. The management plan of the RDSM accounts for more than 5000 lakes in the area, that vary in shape (elongated, circular, and complex), size (from 1.5 ha to 900 ha), and connection to the main rivers and channels, which will influence the lake hydraulic residence and water flow connection during the low water level phase [23].

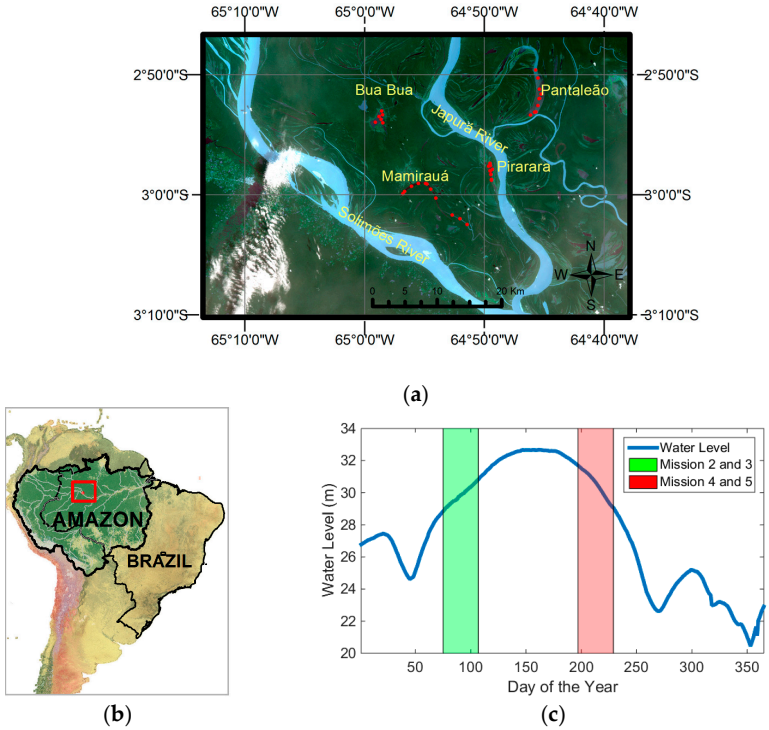

Figure 1. (**a**) OLI true color image for the study area showing the selected lakes inside the MSDR. Red dots represent the distributions of points at each lake. The image is from December 4th of 2014. (**b**) Brazil figure with RDSM location evidenced in red (**c**) Hydrograph for the year 2016, showing water level variation for missions 2, 3 (in green) 4 and 5 (in red). Mission 1 occurred in the same flood phase as missions 4 and 5 in 2015.

The criteria for lake selection included their potential for remote sensing analysis (lake size and shape), as well as accessibility throughout the year. The sampling points were selected to include the main observable changes in the lake water color. Based on the above restrictions, the Bua-Buá (triangular shape, 1 km × 2.1 km), Mamirauá (elongated shape, up to 0.4 km × 4 km), Pirarara (lozengular shape, up to 0.9 km × 2.7 km), and Pantaleão (rectangular shape, up to 1.5 km × 6 km) lakes were selected (Figure 1a).

2.2. In Situ Dataset

Five field missions (subsequently named M1, M2, M3, M4, and M5) were carried out for two years. Missions M2 and M3 were conducted during the rising water period (March and April 2016) and missions M1, M4, and M5 during the receding water period (July 2015, July and August 2016). In each mission, three to six sampling points were visited per lake, resulting in a total of 102 sampling points. At each sampling point, limnological and radiometric data were obtained.

For the limnological measurement, water samples were collected at the subsurface (10 cm) and kept light-free and cooled in ice for a maximum of 3 h, before being filtered. For the Chlorophyll-a concentration (µg/L), water samples were filtered through Whatman GF/F (0.7 µm) filters and for the Total Suspended Solids (TSS) (mg/L) and its Inorganic (TSIS) and Organic (TSOS) fractions, water was filtered through Whatman GF/C (1.2 µm), both of which included 45 mm filters. A maximum of 500 mL was filtered for each sample. Chl-a was analyzed according to Nush [24] and TSS and its fractions according to Wetzel & Likens [25], in replicates.

The Colored Dissolved Organic Matter (CDOM) spectral absorptions ($a_{CDOM}(\lambda)$) (m^{-1}) were determined using a 10 cm quartz cuvette in a single beam mode of the UV-2600 Shimadzu spectrophotometer, scanning from 300 to 800 nm, with 1 nm increments. $a_{CDOM}(\lambda)$ was generated based on the $a_{CDOM}(\lambda)$ measured, following Tilstone et al. [26], and the a_{CDOM} exponential model for each $a_{CDOM}(\lambda)$ measured at 420 nm and the slope of each curve. Table 1 shows the range of magnitude of limnological data, illustrating the optical diversity of the lakes and the changes along the flood pulse.

Table 1. Limnological dataset for each lake and flooding phase. The names refer to the four lakes (Bua-Buá, Mamirauá, Pantaleão, and Pirarara). The mean value is shown followed by the standard deviation in parenthesis. Chl-a is Chlorophyll-a in µg/L, TSS is in mg/L, and a_{CDOM} is $a_{CDOM}(420)$ in m^{-1}.

	Rising Water				Receding Water			
	Bua	**Mam**	**Pant**	**Pira**	**Bua**	**Mam**	**Pant**	**Pira**
Chl-a	14.7 (9.2)	18.1 (6.2)	11 (5.6)	8.3 (3.4)	8.2 (4.9)	7.6 (4.7)	12.1 (5.6)	9.3 (3.6)
TSS	9.5 (3.2)	9.7 (2.6)	18.5 (4.8)	25.9 (6.8)	5.5 (2.4)	5.2 (1.1)	7.5 (1.5)	6.8 (1.3)
a_{CDOM}	5.6 (0.7)	6.4 (1.5)	2.1 (0.2)	2.2 (0.2)	2.5 (0.2)	2.6 (0.3)	2.5 (0.4)	2.1 (0.2)

Radiometric measurements were carried out for all sampling points, using three intercalibrated RAMSES–Trios sensors. The sensors were used to estimate the R_{rs}, above water radiance $(L_w, W{\cdot}m^{-2}{\cdot}sr^1{\cdot}nm^{-1})$, sky radiance $(L_{SKY}, W{\cdot}m^{-2}{\cdot}sr^1{\cdot}nm^{-1})$, and downwelling irradiance $(E_D, W{\cdot}m^{-2}{\cdot}nm^{-1})$, between 350 and 900 nm. During the measurements, the sensors were positioned with azimuth angles between 90° and 135° in relation to the sun and a Zenith angle of 45° to avoid sun glint effects [27]. The measurement framework followed Mobley [28]. All of the measurements were made between 10:00 and 13:00 and at least 15 samples were obtained for each measured depth. The dataset was processed using MSDA_XE and Matlab. The R_{rs} estimate followed Mobley [28], with sun glint correction based on each sampling point spectrum.

Figure 2 shows the R_{rs} magnitude for all of the sampling points, split according to the water stage (rising water Figure 2a and receding water Figure 2b). The threshold conditions influence the

bio-optical properties of the four lakes, with a high input of organic matter throughout the season, especially at Bua-Buá and Mamirauá during the rising water period, whereas Pantaleão and Pirarara's R_{rs} is enhanced by the high sediment loading, particularly during the rising water period. RDSM lakes can be considered dark when compared to sediment loaded inland lakes, making it a remarkable study site to evaluate the impact of the SNR on bio-optical products.

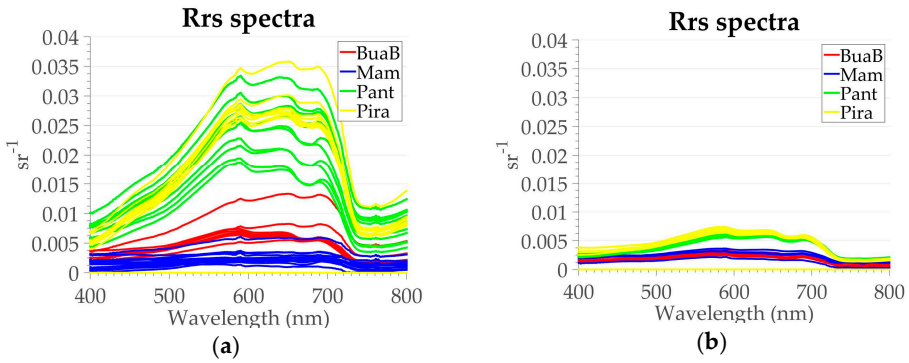

Figure 2. Rrs spectra for each lake in different water phases. (**a**) Mission 2 and 3 (rising water period); (**b**) Mission 1, 4, and 5 (receding water period). Each lake is represented by a specific color; Mamirauá in Blue, Bua-Buá in red, Pantaleão in green, and Pirarara in yellow.

2.3. Data Processing

2.3.1. Dataset Sensor Simulation

The impact of SNR on the R_{rs} spectrum was assessed by simulating two datasets: Noisy spectra and noiseless spectra. The input data for the simulation were in situ measurements and the sensor design specifications. The steps for the simulation are similar for both datasets, except for the noise addition, and are described below. It is important to highlight that the simulation assumes optimum conditions such as perfect atmospheric correction, algorithm calibration, and errorless in situ measurements to isolate the noise impact.

A total of 1000 noisy orbital R_{rs} spectra were simulated for each of the 102 in situ R_{rs} measurements based on the characteristics of MSI/Sentinel-2 [29], OLCI/Sentinel-3 [30], and OLI/Landsat 8 [31], resulting in a total of 306.000 spectra. The simulation workflow (Figure 3) consists of the following five steps: (1) Resampling in situ spectra to sensors that are band-weighted; (2) Computation of a sensor's specific noise; (3) Noise addition to simulated spectra (step 1); (4) Spectra quantization; and (5) Conversion of TOA (Top of atmosphere) irradiance solar spectrum to surface irradiance.

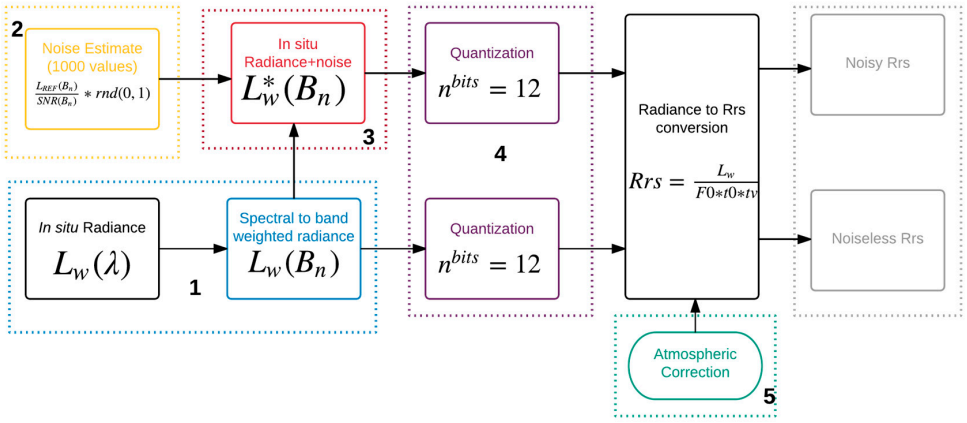

Figure 3. Framework of the proposed simulation for a single spectrum of one orbital sensor.

Image simulation was carried out according to the following steps:

(1) Resampling in situ spectra to sensors that are band-weighted. The conversion of each radiance spectrum to the band-weighted radiance of each sensor was based on the sensor's response function (Tables 2–4), applied according to Equation (1):

$$L_w(B_n) = \frac{\int_{\Delta B_n} L_w(\lambda) \times \mathrm{RF}_{B_n}(\lambda)\mathrm{d}\lambda}{\int_{\Delta B_n} \mathrm{RF}_{B_n}(\lambda)\mathrm{d}\lambda} \quad (1)$$

where B is the sensor band; n is the band number, varying from 1 to n, according to sensor design; $L_w(B_n)$ is the water leaving radiance for each band in the unit of ($\mathrm{W{\cdot}m^{-2}{\cdot}sr^{1}{\cdot}nm^{-1}}$), ΔB_n is the band width; and RF_{B_n} is the response function for each sensor band.

(2) Computation of a sensor's specific noise. The TOA radiance was converted to equivalent noise using the reference radiance at the TOA of each band and sensor (Tables 2–4) and the respective SNR [8] (Equations (2) and (3)).

$$Noise(B_n) = \frac{L_{REF}(B_n)}{SNR(B_n)} \times rnd \quad (2)$$

where L_{REF} is the reference radiance used to generate the specific SNR, SNR is the Signal to Noise Ratio for each sensor band, and rnd is a random number obtained from a standard normal distribution (mean equal to zero and standard deviation equal to one N (0,1)). For each sensor, a total of 1000 $Noise(B_n)$ spectra were generated.

(3) Noise addition to simulated spectra (step 1). The $Noise(B_n)$ was added to the $L_w(B_n)$ Equation (3). To exempt the impact of error propagation due to atmospheric correction on the noise, no atmospheric uncertainty and "optimum" atmospheric correction was assumed.

$$L_w^*(B_n) = L_w(B_n) \pm Noise(B_n) \quad (3)$$

where $L_w^*(B_n)$ is the noisy water leaving radiance for each band.

(4) Spectra quantization. $L_w^*(B_n)$ quantization was carried out according to Equation (4).

$$L_w^{*b}(B_n) = L_w^*(B_n) / \frac{L_{TOA}max(B_n)}{2^{nbit}} \quad (4)$$

where $L_w^{*b}(B_n)$ is the quantized noisy water leaving radiance for each band, $L_{TOA}max(B_n)$ is the maximum radiance measured by the sensor at B_n, and $nbit$ is the number of bits for each sensor (12 bits).

(5) Conversion of TOA (Top of atmosphere) irradiance solar spectrum to surface irradiance. The propagation of the solar spectrum to water level was based on the algorithm described by Vanhellemont & Rudick [10,32], using a standard atmosphere and equations derived from Kaskaoutis & Kambezidis [33], Bird & Riordan [34] and Leckner [35]. The relationship between water leaving radiance (L_w) and reflectance (ρ) is described as:

$$\rho = \frac{\pi \times L_w \times d^2}{F0 \times \cos\theta_0} \quad (5)$$

where d^2 is the Earth-Sun distance in Astronomic Units, θ_0 is the Sun zenith angle, $F0$ is the solar irradiance, and ρ is the reflectance. This paper assumed a value of 1 for d, and $F0$ from Gueymard [36] and Gueymard et al. [37]. $F0$ was propagated to water level as follows [10,32]:

$$F0_{wl} = t_0 \times t_v \times (F0_{TOA}) \quad (6)$$

where t_0 and t_v are the sunwater and sea-sensor diffuse transmittance, $F0_{wl}$ is the solar irradiance at water level, and $F0_{TOA}$ is the solar irradiance at the TOA. For each wavelength, the diffuse transmittance t_0 and t_v was calculated by replacing θ with θ_0 and θ_v in:

$$t = exp\left[-\left(\frac{\tau_r}{2} + \tau_{OZ}\right)/cos\theta\right] \quad (7)$$

where τ_r and τ_{OZ} are the Rayleigh and Ozone optical thickness for a given atmosphere composition, respectively. The impact of water absorption and aerosol absorption on the atmospheric transmittance is ignored in this part of the process.

Table 2. MSI/Sentinel-2 sensor configurations used as the input for simulation. CW is the central wavelength (nm), BW is the band width (nm), SR is the Spatial Resolution (m), L_{REF} ($W{\cdot}m^{-2}{\cdot}sr^{-1}{\cdot}\mu m^{-1}$) is the radiance in which the SNR was calculated, Quant is the quantization, and L_{TOA}max ($W{\cdot}m^{-2}{\cdot}sr^{-1}{\cdot}\mu m^{-1}$) is the maximum radiance that can be measured by the sensor.

Bands	CW	BW	SR	L_{REF}	SNR	Quant	$L_{TOA}max$
B1	443	20	60	129	129	12	588
B2	490	65	10	128	154	12	615.5
B3	560	35	10	128	168	12	559
B4	665	30	10	108	142	12	484
B5	705	15	20	74.5	117	12	449.5
B6	740	15	20	68	89	12	413
B7	783	20	20	67	105	12	387

Table 3. OLCI/Sentinel-3 sensor configurations used as the input for simulation. CW is the central wavelength (nm), BW is the band width (nm), SR is the Spatial Resolution (m), L_{REF} ($W{\cdot}m^{-2}{\cdot}sr^{-1}{\cdot}\mu m^{-1}$) is the radiance in which the SNR was calculated, Quant is the quantization, and L_{TOA}max ($W{\cdot}m^{-2}{\cdot}sr^{-1}{\cdot}\mu m^{-1}$) is the maximum radiance that can be measured by the sensor.

Bands	CW	BW	SR	L_{REF}	SNR	Quant	$L_{TOA}max$
B1	400	10	300	63	2188	12	413.5
B2	412	10	300	74	2061	12	501.3
B3	442	10	300	66	1811	12	466.1
B4	490	10	300	51	1541	12	483.3
B5	510	10	300	44	1488	12	449.6
B6	560	10	300	31	1280	12	524.5
B7	620	10	300	21	997	12	397.9
B8	665	10	300	16	855	12	364.9
B9	673	7.5	300	16	707	12	443.1
B10	681	7.5	300	15	745	12	350.3
B11	708	10	300	13	785	12	332.4
B12	753	7.5	300	10	605	12	377.7
B13	778	15	300	9	812	12	277.5
B14	865	20	300	6	666	12	229.5
B15	885	10	300	6	395	12	281

Table 4. OLI/Landsat 8sensor configurations used as the input for simulation. CW is the central wavelength (nm), BW is the band width (nm), SR is the Spatial Resolution (m), L_{REF} ($W{\cdot}m^{-2}{\cdot}sr^{-1}{\cdot}\mu m^{-1}$) is the radiance in which the SNR was calculated, Quant is the quantization, and L_{TOA}max ($W{\cdot}m^{-2}{\cdot}sr^{-1}{\cdot}\mu m^{-1}$) is the maximum radiance that can be measured by the sensor.

Bands	CW	BW	SR	L_{REF}	SNR	Quant	$L_{TOA}max$
B1	443	20	30	190	232	12	782
B2	482	65	30	190	355	12	800
B3	565	75	30	194	296	12	738
B4	660	50	30	150	222	12	622
B5	867	40	30	150	199	12	381

The Rayleigh optical depth (τ_r) was calculated using the model proposed by Kaskaoutis & Kambezidis [33], with improvements proposed by Leckner [35]:

$$\tau_r\lambda = 0.008735\left(\frac{P}{P0}\right)\lambda^{-4.08} \quad (8)$$

where λ is the wavelength in micrometers, P is the atmospheric pressure at the site (1014 hPa), and $P0$ is the reference sea level pressure (1013.25 hPa).

The t_v was calculated according to Kaskaoutis & Kambezidis [33], which was based on Bird & Riordan [34] and Leckner [35] (Equations (9) and (10)):

$$\tau_v(\lambda) = \exp(\alpha_0 \times \lambda \times O_3 \times M_0) \quad (9)$$

where α_0 is the ozone absorption coefficient, O_3 is the ozone concentration (atm.·cm^{-1}), and M_0 is the ozone mass. The ozone absorption coefficient was linearly interpolated from Bird & Riordan [34], and the ozone mass was calculated following Leckner [35].

$$M_0 = (1 + h_0/6370)\left(cos^2 Z + 2\,h_0/6370\right)^{0.5} \quad (10)$$

where h_0 is the height of the maximum ozone concentration, assumed as 22 km, and Z is the zenithal angle. Input parameters (Tables 5 and 6) were used for solar spectrum propagation throughout the atmosphere.

Table 5. Parameters used during the conversion of the TOA irradiance solar spectrum to surface irradiance for all of the sensors.

Parameter	Range or Value
Date	1 January
Time	12 h 00 min (GMT)
Latitude	0
Ground Elevation	40 m
Sensor Zenith Angle	0
Sensor Azimuth Angle	0
Ozone Amount	0.3 atm cm^{-1}
Height of Maximum Ozone Concentration	22 km
Atmopsheric pressure at site	1014

Table 6. Example of the parameters obtained and used during the atmospheric simulation for the MSI sensor. $F0_{TOA}$ is the band-weighted extraterrestrial solar irradiance, τ_r is the Rayleigh optical thickness for a standard atmosphere, and τ_{OZ} is the ozone optical thickness for 300 DU of atmospheric ozone.

Band	$F0_{TOA}$ (Wm^{-2} μm^{-1})	τ_r	τ_{OZ}
B1 (443)	1938.2	0.2405	0.0004
B2 (490)	1916.5	0.1543	0.0087
B3 (560)	1845.9	0.0934	0.0309
B4 (665)	1524.7	0.0464	0.0167
B5 (705)	1402.5	0.0366	0.0063
B6 (740)	1290	0.0298	0.0030
B7 (783)	1184.8	0.0238	0.0002

The simulation of the noiseless datasets followed the same steps, except for steps 2 and 3.

At the end of the dataset sensor simulation, the quantized noiseless water leaving radiance for each band $\left(L_w^b(B_n)\right)$ and $L_w^{*b}(B_n)$ were converted to $R_{rs}(B_n)$ according to Equation (11), in order to be used as the input for bio-optical algorithms.

$$R_{rs}(B_n) = \frac{L_w^b(B_n)}{F0_{wl}(B_n) \times t_0(B_n) \times t_v(B_n)} \tag{11}$$

where $R_{rs}(B_n)$ is the Remote Sensing Reflectance at B_n, $F0_{wl}$ is the solar irradiance at water level, and t_0 and t_v are the sunwater and sea-sensor diffuse transmittance, respectively.

2.3.2. Impact of Sensors Characteristics on Chl-a and TSS Algorithms

The two simulated datasets (noisy and noiseless) were used to assess the impact of the optical sensor configuration on the Chl-a and TSS algorithms currently in use [38–43]. Seven algorithms were applied for different sensors and study sites [38–43], with few changes in the central wavelengths according to band availability. Algorithms were chosen based on the diversity of bands and mathematical operations involved so as to encompass a range of model equations. For brevity, such models were classified in this paper as additive (subtraction and addition), multiplicative (division and multiplication), and exponential.

Three empirical algorithms were tested for TSS (*TSS_linear*, *TSS_exp*, *TSS_NSSI*) and four algorithms for Chl-a (*CLH*, *2B*, *3B*, *NDCI*) (Table 7). Each algorithm was calibrated using the noiseless dataset and in situ measurements of either TSS or Chl-a. In order to remove the uncertainty of model calibration, the calibrated model was applied to the noiseless dataset, instead of the in situ dataset, and compared with the model results based on the noisy dataset input. This method has two assumptions: (i) the concentration provided by calibrated data is the reference concentration ("ground truth") against which the simulation results are assessed; (ii) the uncertainty between the noisy and noiseless outputs is only due to the changes in SNR. The modeled concentration is compared to the "ground truth", so that changes in magnitude are solely based on two aspects: algorithm constants (e.g., a, b, c, and d (Table 7)) and R_{rs}.

Table 7. Chl-a and TSS algorithms. The exact wavelength used changed for each sensor. *CLH* is a chlorophyll line height model, *2B* is a red/NIR band ratio model, *3B* is a red/NIR 3 band model, *NDCI* is a red NIR 2 band model, *TSS_linear* is a linear red band model, *TSS_exp* is an exponential red band model, and *TSS_NSSI* is a red/green exponential band ratio model.

Model Name	Linear Model ($a \times x + b$)	Reference
CLH	$x = R_{rs}(708) - (R_{rs}(665) + R_{rs}(740))/2$	[38]
2B	$x = R_{rs}(665) \times R_{rs}(708)^{-1}$	[39]
3B	$x = (R_{rs}(665)^{-1} - R_{rs}(708)^{-1}) \times R_{rs}(753)$	[39]
NDCI	$x = R_{rs}(\text{red}) - R_{rs}(\text{NIR})/(R_{rs}(\text{red}) + R_{rs}(\text{NIR}))$	[40]
TSS_linear	$x = R_{rs}(\text{red})$	[41]
	Non Linear model	**Reference**
TSS_exp	$TSS = ((a\ R_{rs}(\text{red}))/b)^c + d$	[42]
TSS_NSSI	$NSSI = (R_{rs}(\text{green}) - R_{rs}(\text{red}))/(R_{rs}(\text{green}) + R_{rs}(\text{red}))$ $TSS = a\ e^{-b\ NSSI}$	[43]

Most approaches employed to quantify the SNR impact on water algorithms use the Normalized Root-Mean-Square Error (NRMSE) (e.g., Moses et al. [8] and Gerace et al. [15]) as a statistic measurement for assessing model quality. Although accuracy measurements such as NRMSE give an insight regarding the proportional error of the model fitting, they do not remove the intrinsic error due to the choice of algorithm equations, which might lead to an over- or underestimation of SNR error. For this reason, this paper focuses on the relationship between the algorithm equation, R_{rs} magnitude,

and the shape of the modeled concentration distribution. Considering the available bands for each sensor, Chl-a algorithms were applied to MSI and OLCI sensors, while TSS algorithms were applied to the three sensors.

3. Results and Discussion

3.1. Dataset Simulation

The simulated R_{rs} values for the three sensors and the relative error are shown in Figure 4. Given the sensor design, OLCI (Figure 4c) presented the highest spectral resolution and number of bands, allowing an accurate portrayal of the water R_{rs} spectrum. On the other hand, the spatial resolution (300 m) limits its application in the study of small and narrow lakes, as opposed to OLI and MSI (up to 30 m).

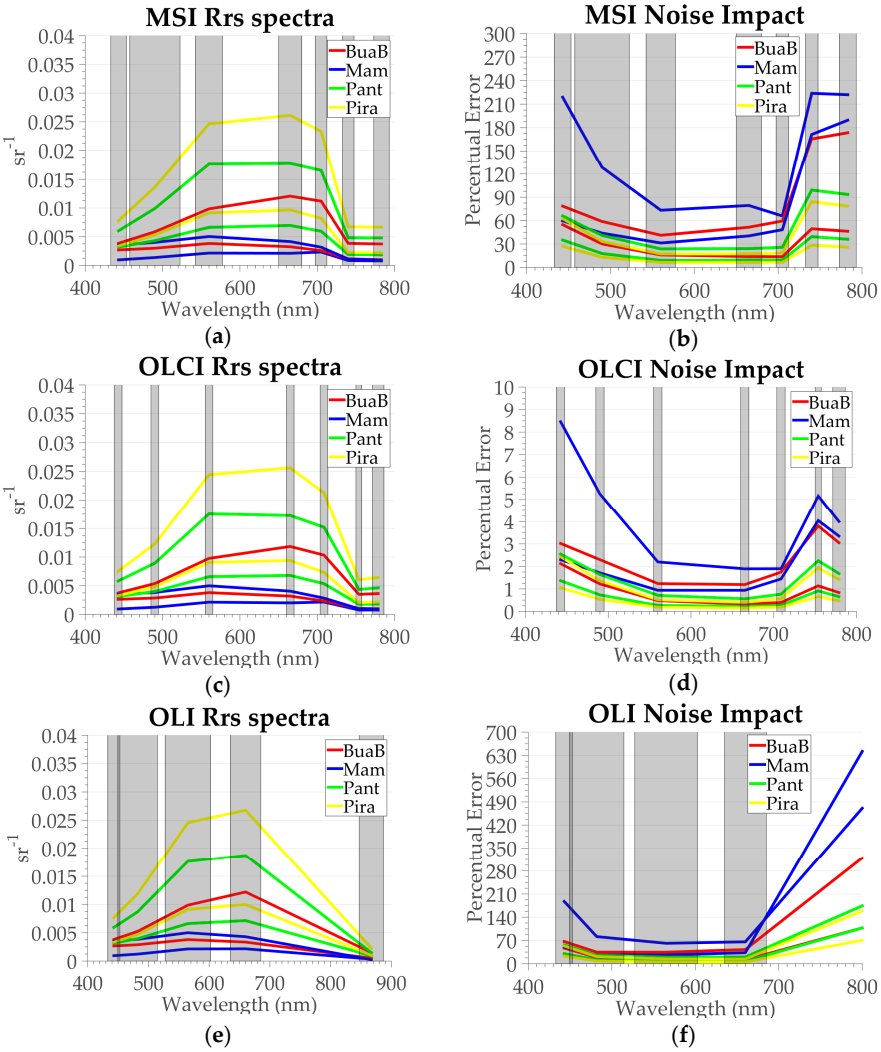

Figure 4. (**a**–**f**) Noise band-weighted R_{rs} spectra for each sensor (**a**,**c**,**e**) and normalized error due to the optical characteristics of each sensor band (**b**,**d**,**f**), with two spectra of each lake. (**a**,**b**) MSI; (**c**,**d**) OLCI; (**e**,**f**) OLI. Each lake is represented by a specific color; Mamirauá in Blue, Bua-Buá in red, Pantaleão in green, and Pirarara in yellow. The noise used was equal to $\frac{L_{TOA}}{SNR} \times .rnd$, in which *rnd* is the standard deviation of a standard normal distribution (equal to 1). The percent error is equal to $100 \times \frac{R_{rs}(noisy) - R_{rs}}{R_{rs}}$.

Disregarding the sensor design, the error percentage due to noise is higher in the blue and NIR bands (Figure 4b,d,f) than that in the remaining bands. The relative high impact in the blue band is

due to the higher signal from the atmosphere in relation to longer wavelengths. In the Near Infra-Red (NIR) band, nevertheless, the relative error is due to the small SNR (Tables 2–4). OLI has the highest relative noise impact, reaching 700% in the NIR, whereas MSI's maximum value is 250% and OLCI's maximum value is only 10%. Considering these results, the best algorithms for the retrieval of optical components should include bands between 550 and 700 nm, where relative errors are below 50% in all of the cases. Another important aspect is the relative error for each lake, as a function of water clarity. The highest errors are observed at Mamirauá and Bua-Buá (dark lakes), while the errors at Pirarara and Pantaleão (bright lakes) are below 50% for all bands. The results indicate that before selecting the sensor, it is crucial to consider the R_{rs} amplitude range, as long as the spatial resolution suits the lake area and shape constraints.

3.2. Algorithm Evaluation

3.2.1. Chlorophyll-a

The results show that the relative accuracy of Chl-a retrieval is highly dependent on the model equation, SNR, and R_{rs} magnitude (Figures 5 and 6). In general, the concentration error increases from additive towards multiplicative band operations. Additionally, the highest error for all of the models was observed for the MSI sensor. Although the bandwidth and position are additional sources of uncertainty for algorithms, this method compared the noisy and noiseless datasets of each sensor, assuming that error amplitude is only related to the SNR of each sensor.

In the *CLH* model, the relationship among the bands is additive, so the noise impact is reduced when compared to the multiplicative models (Figures 5 and 6). The concentration error is affected by the algorithm slope, while the intercept contribution is constant for all concentrations. The error magnitude and distribution (Figures 5a and 6a) are the same for all concentrations; so, a higher relative error is expected for low concentrations due to the algorithm intercept uncertainty. For these algorithms, the concentration changes do not depend on the R_{rs} magnitude.

A different pattern is observed for the multiplicative Chl-a algorithms (*2B*, *3B*, *NDCI*–Figures 5 and 6b–d) which apply band ratios. In this case, the noise interference can be either constructive or destructive. When compared to the additive model (*CLH*), a higher error amplitude is expected for all concentrations. The highest relative impact is observed in low concentrations.

The SNR impact on the Chl-a concentration changes according to the model equation (Figures 5 and 6). Most approaches quantifying the SNR impact on water algorithms use RMSE or NRMSE. For example, Moses et al. [8] observed sensor relative errors of up to 40% for the OC4 algorithm and 25% for the two bands red-NIR algorithm for HICO. Gerace et al. [15] used an optimization algorithm for OLI and MERIS and observed errors of 35% for Chl-a. These errors, however, were computed assuming that the R_{rs} magnitude, model equation, and noise are independent. Based on our results and given that OC4 is a fourth-degree polynomial (not tested in this work), one would expect a higher error amplitude in Chl-a estimates due to the SNR.

For the *CLH* model, the error amplitude changed for each sensor, but its distribution shape remained the same. The error amplitude is constant for all concentrations, with a value of around 1 µg/L for MSI and 0.1 µg/L for OLCI. The relative error is higher for low concentrations (up to 11%) and is halved at the max concentration (Figures 5 and 6a).

For the *2B*, *3B*, and *NDCI* models, the shape of the noisy data distributions seems to be erratic, with different amplitudes for similar concentrations for the three sensors (Figures 5 and 6b–d). The analysis of the in situ spectrum for model *2B*, *3B*, and *NDCI*, showed a higher error amplitude (up to 2 µg/L) for spectra with a low R_{rs} magnitude (<0.005 sr^{-1}) (Figure 7a). On the other hand, for spectra with a higher R_{rs} (>0.01 sr^{-1}) (Figure 7b), the amplitude is similar to that of the *CLH* model. Based on these results, the impact of the SNR on the Chl-a estimation is higher in dark lakes such as Mamirauá and Bua-Buá (errors of up to 2 µg/L) (Figure 7c,d) for OLCI. For the MSI sensor, the three proposed algorithms showed a higher impact than that of OLCI due to the poorer SNR, with errors above 10 µg/L.

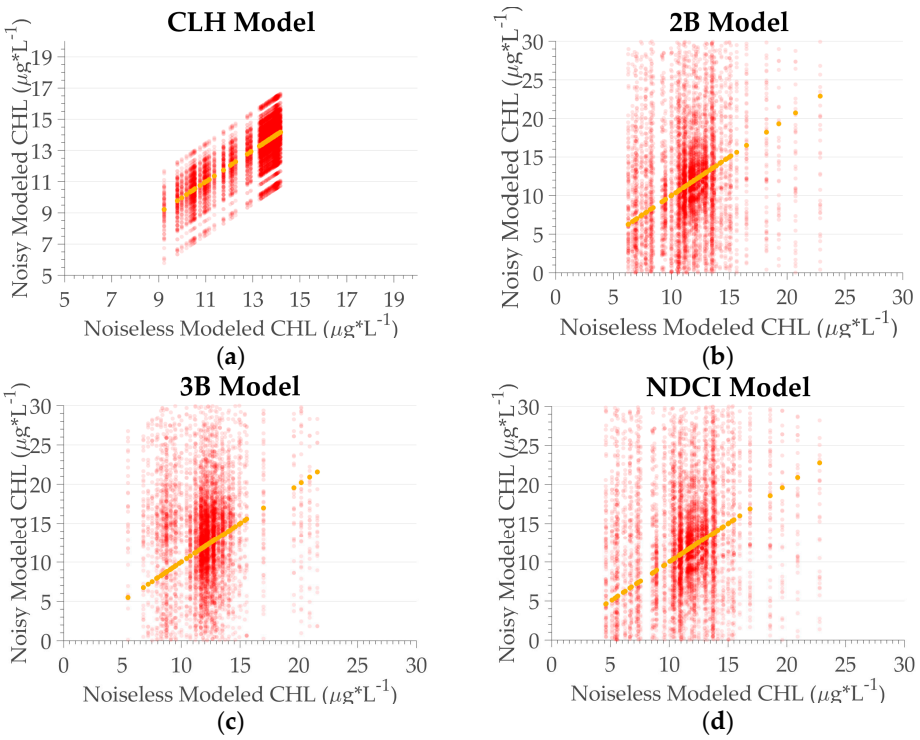

Figure 5. Algorithm performance for the chl-a concentration of the MSI sensor. (**a**) *CLH*; (**b**) *2B*; (**c**) *3B*; (**d**) *NDCI*. Circles in red represent the data with noise, circles in yellow the noiseless data. The transparency is based on the frequency distribution, in which opaque indicates a higher frequency, and transparent indicates a lower frequency.

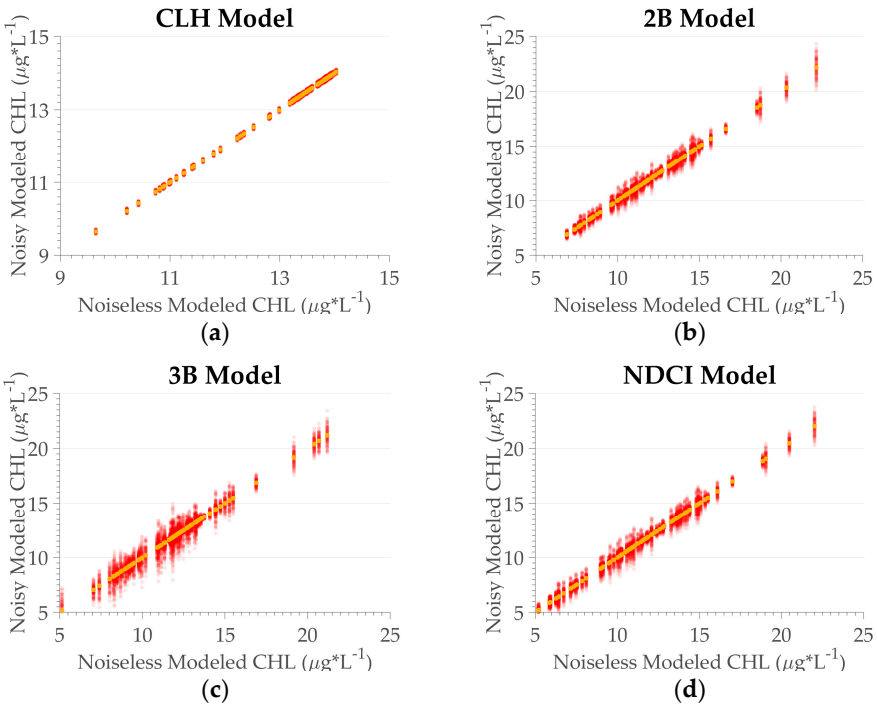

Figure 6. Algorithm performance for the chl-a concentration of the OLCI sensor. (**a**) *CLH*; (**b**) *2B*; (**c**) *3B*; (**d**) *NDCI*. Circles in red represent the data with noise, circles in yellow the noiseless data. The transparency is based on the frequency distribution, in which opaque indicates a higher frequency, and transparent indicates a lower frequency.

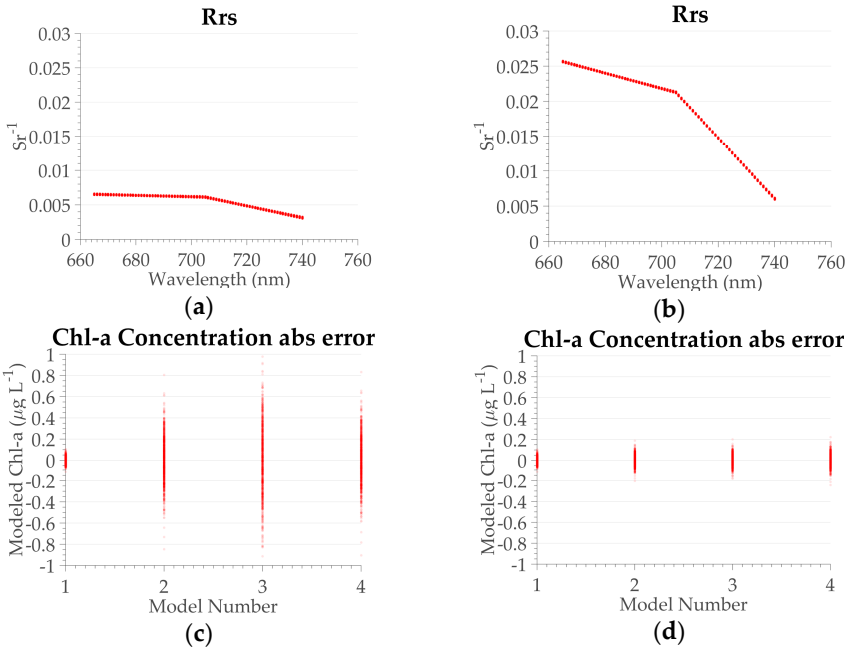

Figure 7. Example of the OLCI R_{rs} magnitude and Chl-a concentration obtained for the four models for two lakes. (**a**) R_{rs} for three bands for one sample station of Bua-Buá, (**b**) R_{rs} for three bands for one sample station of Pirarara, (**c**) Chl-a concentration for the Bua-Buá sampling point, (**d**) Chl-a concentration for the Pirarara sampling point. The numbers 1, 2, 3, and 4 refer to the *CLH*, *2B*, *3B*, and *NDCI* models, respectively.

For spectra with a low R_{rs}, the error distribution amplitude was higher than those with a high R_{rs}. Therefore, future sensors for imaging inland water applications should require both a higher SNR minimum and minimum spatial resolution to cope with small and narrow lakes. Another aspect to be considered is the model equation. According to Luck [44], higher order algorithms increase the fitness between in situ and modeled data. However, these algorithms propagate the uncertainty in Chl-a estimates due to the SNR under specific conditions (e.g., low R_{rs} magnitude and model equation), decreasing the algorithm accuracy. Thus, the balance of those two aspects should also be considered when applying water quality algorithms, as shown by the results from the four models (Figures 5–7).

As the *CLH* model uses an additive operation, it can be applied to the four lakes using the three sensors, without any preprocessing. For the multiplicative models, however, spatial resampling may be necessary in order to mathematically increase the SNR. For example, with a 2 × 2 and 3 ×3 pixel window, it is possible to increase the SNR by up to two and three times, respectively. These SNR increments can be calculated by the square root of the window size times the original SNR [45]. In the case of MSI, the pixel size of the selected bands is up to 30 m, so resampling may computationally increase the SNR without compromising the results for suitable sized lakes. On the other hand, an OLCI 300 m pixel size is not appropriate for resampling for most of the small lakes due to spectral mixing [46]. Therefore, when comparing the design of sensors for inland water application, it is imperative to assess the sensor suitability for any specific study site, as well as the post processing feasibility (if required).

3.2.2. TSS

Similarly to Chl-a algorithms, the relative accuracy of TSS retrieval depends on the model equation, SNR, and R_{rs} magnitude (Figures 8–10. In general, the TSS concentration error increases from additive to multiplicative equations and from linear to exponential models.

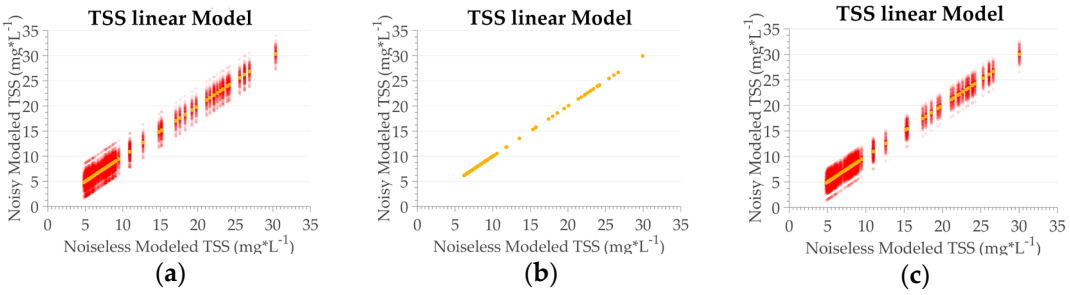

Figure 8. *TSS_linear* model performance for TSS concentration. (**a**) MSI sensor; (**b**) OLCI sensor; (**c**) OLI sensor. Circles in red represent the data with noise, circles in yellow noiseless data. The transparency is based on the frequency distribution, in which opaque indicates a higher frequency, and transparent indicates a lower frequency.

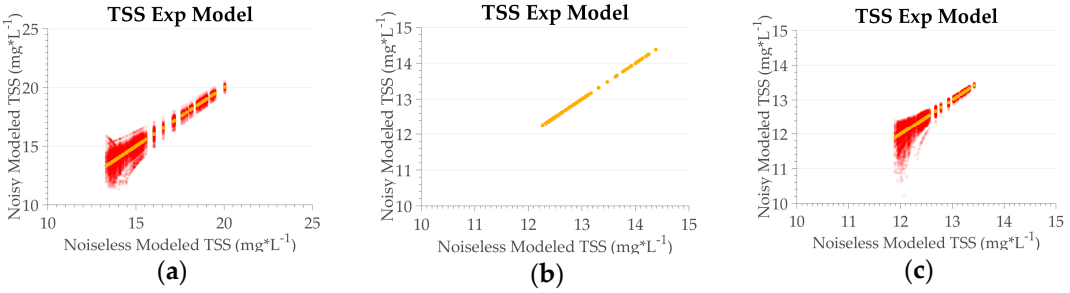

Figure 9. *TSS_exp* algorithm performance for TSS concentration. (**a**) MSI sensor; (**b**) OLCI sensor; (**c**) OLI sensor. Circles in red represent the data with noise, circles in yellow noiseless data. The transparency is based on the frequency distribution, in which opaque indicates a higher frequency, and transparent indicates a lower frequency.

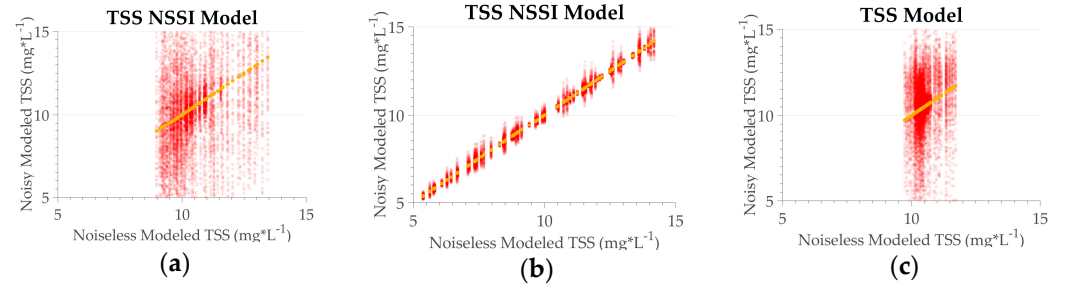

Figure 10. *TSS_NSSI* algorithm performance for TSS concentration. (**a**) MSI sensor; (**b**) OLCI sensor; (**c**) OLI sensor. Circles in red represent the data with noise, circles in yellow noiseless data. The transparency is based on the frequency distribution, in which opaque indicates a higher frequency, and transparent indicates a lower frequency.

For the *TSS_linear* model (Figure 8), the noise impact is linear for all the sensors and throughout the concentration range. The highest error is observed for the MSI sensors (5 mg/L), followed by OLI (3 mg/L) and OLCI (negligible error). The relative contribution of the error is higher with low concentrations. Given that the absolute impact of the noise is constant throughout the concentrations, the relative error is lower for higher concentrations. For the *TSS_exp* model (Figure 9), a distinct pattern is observed; in low TSS concentrations, the error is higher, and the distribution follows an exponential curve towards a higher concentration. The maximum errors for the *TSS_exp* model reach 3 mg/L and 1 mg/L for MSI and OLI, respectively (Figure 9). Lastly, the *TSS_NSSI* model (Figure 10) showed an

erratic pattern, similar to that displayed in the Chl-a multiplicative models (Figure 6b–d), suggesting a dependency on the R_{rs} magnitude due to the band ratio approach.

Moses et al. [8] found similar results for HICO, with errors of up to 40% for concentrations below 3 mg/L, and up to 5% for concentrations above 5 mg/L. Although the authors used the optimized error minimization approach, the results displayed similar patterns as observed in this study. Gerace et al. [15] observed mean errors of up to 15% due to the SNR in TSS algorithms.

The uncertainty in the TSS retrieval due to the SNR is highly dependent on the model. The model equation and the concentration range control the need of pixel resampling in order to reduce the noise impact. An MSI and OLI pixel size of 30 m is adequate for most lakes, but the SNR can be a limitation. One band model is usually enough for TSS retrieval, so the OLI spectral resolution is not a restriction, but the SNR, in some cases, needs to be mathematically increased similarly to Chl-a algorithms. In spite of the good congruence of the OLCI estimates, its pixel size of 300 m is a serious constraint for the study of small lakes, as for those in the RDSM.

4. Conclusions

The experiment carried out to assess the impact of the SNR on water color products indicated that, regardless of the estimated parameter (TSS or Chl-a) and sensor design (OLI, OLCI, and MSI), the error pattern is similar for any given algorithm. It is important to highlight that the simulation assumes optimum conditions such as perfect atmospheric correction, algorithm calibration, and errorless in situ measurements to isolate the noise impact. For an actual orbital image, under the described suboptimal conditions, there is an increase in the uncertainty of TSS and Chl-a retrievals.

The amplitude of the retrieved concentration due to the noise is constant for the entire concentration range when using additive and single band algorithms. However, when using multiplicative algorithms, the amplitude changes according to the model equation and to the R_{rs} magnitude. Finally, we observed that the retrieval amplitude is higher for a low concentration regarding the exponential algorithm.

The noise impact on band ratio algorithms applied to Chl-a and TSS retrieval is amplified when using a lower R_{rs}. While this impact is less substantial for a higher R_{rs}, it is similar to that of the additive algorithms. Although the OLCI sensor presents the best performance due to its narrow band width and high SNR (error of up to 2 μg/L for Chl-a and 3 mg/L for TSS), its spatial resolution (300 m) can be restrictive to most remote sensing studies in RDSM.

For the MSI sensor, despite its low SNR, the error magnitudes of the linear single bands algorithm used to retrieve the TSS and additive algorithms for Chl-a are low (up to 5 mg/L and 1 μg/L, respectively). Even though multiplicative algorithms using MSI data to retrieve Chl-a presented an error above 10 μg/L, the sensor could be applied if the lake size and shape enable resampling.

The OLI simulation indicated that its design is slightly better than that of MSI for all TSS algorithms, resulting in errors below 3 mg/L and 5 mg/L, respectively. However, the number and position of OLI bands are clear restrictions for Chl-a retrieval.

The sensor and algorithm selection need a comprehensive analysis before inland water studies are carried out. In this analysis, the sensor design, in situ conditions (cloud cover, lake size/ shape, and adjacency effects), water brightness (R_{rs}), and model equation (mathematical operation and fitting model) are the key factors considered.

The methods developed in this study will be applied in the near future under real conditions, in order to investigate the role of each of those aspects on the uncertainty caused by the real noise on bio-optical products.

Acknowledgments: This study was funded by the São Paulo Research Foundation (FAPESP) from project no.: 597 2014/23903-9, National Council for Scientific and Technological Development (CNPq) from project no.: 461469/2014-6, and MSA-BNDES from project no.: 1022114003005. Jorge was funded by the CNPq. We are very grateful to Vitor Martins, Renato Ferreira, Jean Farhat, Franciele Sarmento, and Waterloo Pereira Filho for their assistance during field missions. We would like to thank the Mamirauá Institute and staff for all the support during those two years.

Author Contributions: Daniel S. F. Jorge, Claudio C. F. Barbosa, Lino A. S. de Carvalho, Adriana G. Affonso, Felipe de L. Lobo, and Evlyn M. L. M. Novo designed the research. Daniel S. F. Jorge performed the simulation and wrote the paper. Daniel S. F. Jorge, Claudio C. F. Barbosa, Lino A. S. de Carvalho, and Adriana G. Affonso were involved in the collection of field data. Claudio C. F. Barbosa and Lino A. S. de Carvalho supported the development of the Matlab routines used in the proposed methodology. All authors contributed insights for the analysis and methodology, and equally contributed towards organizing and reviewing the manuscript.

Conflicts of Interest: The authors declare no conflict of interest.

References

1. IOCCG. *Minimum Requirements for an Operational Ocean-Colour Sensor for the Open Ocean*; Reports of the International Ocean-Colour Coordinating Group, No. 1; IOCCG: Dartmouth, NS, Canada, 1997.
2. Martins, V.S.; Barbosa, C.C.F.; de Carvalho, L.A.S.; Jorge, D.S.F.; Lobo, F.L.; Novo, E.M.L.M. Assessment of Atmospheric Correction Methods for Sentinel-2 MSI Images Applied to Amazon Floodplain Lakes. *Remote Sens.* **2017**, *9*, 322. [CrossRef]
3. Brando, V.E.; Decker, A.G. Satellite hyperspectral remote sensing for estimating estuarine and coastal water quality. *IEEE Trans. Geosci. Remote Sens.* **2003**, *41*, 1378–1387. [CrossRef]
4. Gao, B.C.; Montes, M.J.; Davis, C.O.; Goetz, A.F.H. Atmospheric correction algorithms for hyperspectral remote sensing data of land and ocean. *Remote Sens. Environ.* **2009**, *113*, S17–S24. [CrossRef]
5. Chen, J.; Lee, Z.; Hu, C.; Wei, J. Improving satellite data products for open oceans with a scheme to correct the residual errors in remote sensing reflectance. *J. Geophys. Res. Oceans* **2016**, *121*, 3866–3886. [CrossRef]
6. Giardino, C.; Bresciani, M.; Cazzaniga, I.; Schenk, K.; Rieger, P.; Braga, F.; Matta, E.; Brando, V.E. Evaluation of Multi-Resolution Satellite Sensors for Assessing Water Quality and Bottom Depth of Lake Garda. *Sensors* **2014**, *14*, 24116–24131. [CrossRef] [PubMed]
7. Braga, F.; Giardino, C.; Bassani, C.; Matta, E.; Candiani, G.; Strömbeck, N.; Adamo, M.; Bresciani, M. Assessing water quality in the northern Adriatic Sea from HICO™ data. *Remote Sens. Lett.* **2013**, *4*, 1028–1037. [CrossRef]
8. Moses, W.J.; Bowles, J.H.; Lucke, R.L.; Corson, M.R. Impact of signal-to-noise ratio in a hyperspectral sensor on accuracy of biophysical parameter estimation in case II waters. *Opt. Express* **2012**, *20*, 4309–4330. [CrossRef] [PubMed]
9. Pahlevan, N.; Lee, Z.; Wei, J.; Schaaf, C.B.; Schott, J.R.; Berk, A. On-orbit radiometric characterization of OLI (Landsat-8) for applications in aquatic remote sensing. *Remote Sens. Environ.* **2014**, *154*, 272–284. [CrossRef]
10. Vanhellemont, Q.; Ruddick, K. Advantages of high quality SWIR bands for ocean color processing: Examples from Landsat-8. *Remote Sens. Environ.* **2015**, *161*, 89–106. [CrossRef]
11. Lobo, F.L.; Novo, E.M.L.M.; Barbosa, C.C.F.; Galvão, L.S. Reference spectra to classify Amazon water types. *Int. J. Remote Sens.* **2012**, *33*, 3422–3442. [CrossRef]
12. IOCCG. *Remote Sensing of Ocean Colour in Coastal, and Other Optically-Complex Waters*; Sathyendranath, S., Ed.; Reports of the International Ocean-Colour Coordinating Group, No. 3; IOCCG: Dartmouth, NS, Canada, 2000.
13. Mouw, C.B.; Greb, S.; Aurin, D.; DiGiacomo, P.M.; Lee, Z.; Twardowski, M.; Binding, C.; Hu, C.; Ma, R.; Moor, T.; et al. Aquatic color radiometry remote sensing of coastal and inland waters: Challenges and recommendations for future satellite missions. *Remote Sens. Environ.* **2015**, *160*, 15–30. [CrossRef]
14. Palmer, S.C.J.; Kutser, T.; Hunter, P.D. Remote sensing of inland waters: Challenges, progress and future directions. *Remote Sens. Environ.* **2015**, *157*, 1–8. [CrossRef]
15. Gerace, A.D.; Schott, J.R.; Nevins, R. Increased potential to monitor water quality in the near-shore environment with Landsat's next-generation satellite. *J. Appl. Remote Sens.* **2013**, *7*, 073558. [CrossRef]
16. Junk, W.J.; Bayley, P.B.; Sparks, R.E. The flood pulse concept in river-floodplain systems. *Can. Spec. Publ. Fish. Aquat. Sci.* **1989**, *106*, 110–127.
17. Queiroz, H.L. A reserva de desenvolvimento sustentável Mamirauá. *Estudos Avançados* **2005**, *19*, 183–203. [CrossRef]
18. Ayres, J.M. *As Matas de Várzea do Mamirauá Médio Rio Solimões*; CNPq-Programa Trópico Úmido e Sociedade Civil Mamirauá: Brasília, Brasil, 1993; p. 123.
19. Queiroz, H.L. Classification of water bodies based on biotic and abiotic parameters at the várzeas of Mamirauá Reserve, Central Amazon. *Uakari* **2007**, *3*, 19–34.

20. Ramalho, E.E.; Macedo, J.; Vieira, T.M.; Valsecchi, J.; Calvimontes, J.; Marmontel, M.; Queiroz, H. Ciclo hidrológico nos ambientes de várzea da Reserva de Desenvolvimento Sustentável Mamirauá: Médio Rio Solimões, período de 1990 a 2008. *Uakari* **2009**, *5*, 61–87.
21. Melack, J.M.; Bruce, R.F. Biogeochemistry of Amazon Floodplain. In *The Biogeochemistry of the Amazon Basin*; Oxford University Press: New York, NY, USA, 2001; p. 235.
22. Forsberg, B.R.; Devol, A.H.; Rickey, J.E.; Martinelli, L.A.; Santos, H. Factors controlling nutrient concentrations in Amazon floodplain lakes. *Limnol. Oceanogr.* **1988**, *33*, 41–56. [CrossRef]
23. Affonso, A.G.; Queiroz, H.; Novo, E.M.M.L. Change in macrophyte coverage may affect pirarucu (*Arapaima gigas*) abundance, fishery and conservation in Amazon floodplain lake. In Proceedings of the 6th World Fisheries Congress, Edinburgh, UK, 7–12 May 2012.
24. Nush, EA. Comparison of different methods for chlorophyll and phaeopigment determination. *Arch. Hydrobiol.* **1980**, *14*, 14–39.
25. Wetzel, R.G.; Likens, G.E. *Limnological Analyses*; Springer: New York, NY, USA, 1991; p. 391.
26. Tilstone, G.H.; Moore, G.F.; Sorensen, K.; Doerffer, R.; Rottgers, R.; Ruddick, K.; Pasterkamp, R.; Jorgensen, P.V. REVAMP Regional validation of MERIS chlorophyll products in North. Sea coastal waters. In Proceedings of the Working meeting on MERIS and AATSR Calibration and Geophysical Validation (ENVISAT MAVT-2003), Frascati, Italy, 20–24 October 2003.
27. Mueller, J.L.; Fargion, G.S. *Ocean Optics Protocols for Satellite Ocean Color Sensor Validation*; Revision 3; NASA TM 2002-210004; NASA Goddard Space Flight Center: Greenbelt, MD, USA, 2002; p. 308.
28. Mobley, C.D. Estimation of the remote-sensing reflectance from above-surface measurements. *Appl. Opt.* **1999**, *38*, 7442–7455. [CrossRef] [PubMed]
29. ESA Sentinel Online. Sentinel-2 MSI Introduction. Available online: https://earth.esa.int/web/sentinel/user-guides/sentinel-2-msi (accessed on 26 February 2017).
30. ESA Sentinel Online. Sentinel-3 OLCI Introduction. Available online: https://earth.esa.int/web/sentinel/user-guides/sentinel-3-olci (accessed on 26 February 2017).
31. OSCAR Observing Systems Capability Analysis and Review Tool. Available online: www.wmo-sat.info/oscar/instruments/view/375 (accessed on 26 February 2017).
32. Vanhellemont, Q.; Ruddick, K. Turbid wakes associated with offshore wind turbines observed with Landsat 8. *Remote Sens. Environ.* **2014**, *145*, 105–115. [CrossRef]
33. Kaskaoutis, D.G.; Kambezidis, H.D. Investigation into the wavelength dependence of the aerosol optical depth in the Athens area. *Q. J. R. Meteorol. Soc.* **2006**, *132*, 2217–2234. [CrossRef]
34. Bird, R.; Riordan, C. Simple Solar Spectral Model for Direct and Diffuse Irradiance on Horizontal and Tilted Planes at the Earth's Surface for Cloudless Atmospheres. *J. Clim. Appl. Meteorol.* **1984**, *25*, 87–97. [CrossRef]
35. Leckner, B. The spectral distribution of solar radiation at the earth's surface elements of a model. *Sol. Energy* **1978**, *20*, 143–150. [CrossRef]
36. Gueymard, C. Parameterized transmittance model for direct beam and circumsolar spectral irradiance. *Sol. Energy* **2001**, *71*, 325–346. [CrossRef]
37. Gueymard, C.; Myers, D.; Emery, K. Proposed reference irradiance spectra for solar energy systems testing. *Sol. Energy* **2002**, *73*, 443–467. [CrossRef]
38. Matthews, M.W.; Bernard, S.; Robertson, L. An algorithm for detecting trophic status (chlorophyll-a), cyanobacteria-dominance, surface scums and floating vegetation in inland and coastal waters. *Remote Sens. Environ.* **2012**, *124*, 637–652. [CrossRef]
39. Moses, W.J.; Gitelson, A.A.; Berdinikov, S.; Povazhnyy, V. Satellite estimation of chlorophyll-a concentration using the red and NIR bands of MERIS-the Azov Sea case study. *IEEE Geosci. Remote Sens. Lett.* **2009**, *6*, 845–849. [CrossRef]
40. Mishra, S.; Mishra, D.R. Normalized difference chlorophyll—A retrieval in turbid, productive estuaries: Chesapeake Bay case study. *Remote Sens. Environ.* **2007**, *109*, 464–472.
41. Binding, C.E.; Bowers, D.G.; Mitchelson-Jacob, E.G. An algorithm for the retrieval of suspended sediment concentrations in the Irish Sea from SeaWiFS ocean colour satellite imagery. *Int. J. Remote Sens.* **2003**, *24*, 3791–3806. [CrossRef]
42. Chen, X.; Han, X.; Feng, L. Towards a practical remote-sensing model of suspended sediment concentrations in turbid waters using MERIS measurements. *Int. J. Remote Sens.* **2015**, *36*, 3875–3889. [CrossRef]

43. De Lucia Lobo, F.; Costa, M.P.; Leao de Moraes Novo, E.M. Time-series analysis of Landsat-MSS/TM/OLI images over Amazonian waters impacted by gold mining activities. *Remote Sens. Environ.* **2015**, *157*, 170–184. [CrossRef]
44. Friedman, J.; Hastie, T.; Tibshirani, R. *The Elements of Statistical Learning*; Series in Statistics; Springer: Berlin, Germany, 2001; Volume 1.
45. Luck, S.J. *An Introduction to the Event-Related Potential Technique*; MIT Press: Cambridge, MA, USA, 2014.
46. Roberts, D.A.; Gardner, M.; Church, R.; Ustin, S.; Scheer, G.; Green, R.O. Mapping chaparral in the Santa Monica Mountains using multiple endmember spectral mixture models. *Remote Sens. Environ.* **1998**, *65*, 267–279. [CrossRef]